applied sciences

MDPI

Article

Copper Alloys Performance in High-Pressure and Low-Velocity Conditions Using a Custom Tribometer

Márcio Rodrigues da Silva [1,2,*], Vinícius Torres dos Santos [2], Flávia Gonçalves Lobo [2], Daniel Ayarroio Seixas [2] and Izabel Fernanda Machado [1]

[1] Surface Phenomena Laboratory, Escola Politécnica da Universidade de São Paulo, São Paulo 05508-010, Brazil; machadoi@usp.br
[2] Centro de Pesquisa, Desenvolvimento e Ensaios da Termomecanica São Paulo S.A., São Paulo 09612-000, Brazil; vinicius.santos@termomecanica.com.br (V.T.d.S.); flavia.lobo@termomecanica.com.br (F.G.L.); daniel.seixas@termomecanica.com.br (D.A.S.)
* Correspondence: marcio.rodrigues@termomecanica.com.br

Abstract: A custom tribometer was developed to measure friction coefficient and temperature in high-pressure, low-velocity conditions, specifically for studying copper alloys used in sliding bearings for heavy equipment. Using this equipment, two commercial alloys were tested to evaluate friction coefficient, specific wear rate, thermal behavior, and subsurface strain. The results, validated through comparison with reference commercial equipment and uncertainty estimates, met acceptable criteria for tribological tests, with an uncertainty estimate value for the friction coefficient of 0.4%. The tribological tests confirmed the importance of solid lubrication in high-lead bronzes and the high wear resistance of Cu-Al-Ni-Fe alloys, which directly influence temperature, subsurface strain, and respective wear mechanisms.

Keywords: tribometer; tribology; copper; bronze; solid lubrication; Cu-Al-Ni-Fe bronze alloys

Citation: da Silva, M.R.; dos Santos, V.T.; Lobo, F.G.; Seixas, D.A.; Machado, I.F. Copper Alloys Performance in High-Pressure and Low-Velocity Conditions Using a Custom Tribometer. *Appl. Sci.* **2024**, *14*, 6001. https://doi.org/10.3390/app14146001

Academic Editor: Guian Qian

Received: 22 May 2024
Revised: 20 June 2024
Accepted: 3 July 2024
Published: 10 July 2024

1. Introduction

Journal sliding bearings are machine elements designed to transmit loads or reaction forces from a shaft with an essentially radial reaction force. Sliding bearings are superior to roller or ball bearings, especially in heavy machinery applications, because they require less space and are more cost-effective. Most of this equipment operates at high load and low velocity. This combination inevitably leads to boundary lubrication, where a thin layer of lubricant forms but does not fully separate the surfaces, and dry sliding, where there is no lubricant and direct contact between the shaft and journal bearing materials occurs [1–4].

Dry sliding predictably increases surface interaction, leading to a higher friction coefficient (μ) and surface wear. Consequently, more surface interactions increase heat per area generation (q). The magnitude of q can be determined by Equation (1), where μ is the friction coefficient, W is the applied normal load, A is the bearing contact area, P is the contact pressure, and V is the sliding velocity [1,5,6]:

$$q = \mu \cdot \frac{W}{A} \cdot V = \mu \cdot P \cdot V \quad (1)$$

The increase in temperature caused by heat transfer through conduction can potentially impact the performance of the plain bearing surface while in use. Therefore, assessing the energy generation per area with the contact pressure (P) and sliding speed (V) (the PV Factor) is useful for evaluating the bearing conditions. Equation (2) allows one to establish a relationship between the PV factor conditions as a function of the surface temperature

increase (ΔT), the thermal conductivity of sliding bearing material (k_T), and the thickness of the bearing base material (s) [1,6].

$$P \cdot V = \frac{k_T}{\mu \cdot s} \cdot \Delta T \quad (2)$$

When evaluating (2), it is essential to consider situations with high pressures and/or velocities, i.e., higher PV factors. These situations require bearing materials with high thermal conductivity, low friction coefficients, and the ability to withstand high surface temperatures. This gradually brings greater importance to the correct selection of journal-bearing material. In this context, copper alloys have been historically extensively used in bearing bushings since the first steam engines, mainly due to the high thermal conductivity associated with low friction coefficient values when in contact with ferrous alloys. In the present context, it is worth emphasizing two significant types of alloys: high-lead tin bronzes and nickel aluminum bronzes [2,6–8].

High-lead tin bronze alloys, containing up to 30% lead by weight, stand out as one of the most suitable alloys for the intended purpose. The insolubility of lead in the CuSn matrix gives rise to a microstructure consisting of successive copper-rich matrices interspersed with low-shear strength lead "sponges", being the main reason to employ alloys with the most significant lead content possible, resulting in a self-lubrication mechanism triggered by the extrusion of lead inclusions [7–13].

Copper-aluminum-nickel-iron (CuAlNiFe) alloys, known as nickel aluminum bronze (NAB), contain around 5% wt. nickel and iron, which causes the intentional formation of κ (kappa) phases. Although they do not have self-lubricating properties, these alloys are a popular choice for journal bearings that operate in harsh environments, as they offer higher strength, wear, and corrosion resistance and can withstand elevated temperatures that often exceed 260 °C. However, while these alloys have excellent mechanical resistance, they tend to have lower ductility and require specific care regarding surface finishing, assembly alignment, and lubricating oil cleaning [2,8,14–20].

Tribology studies are fundamental to accessing enhanced performance and new copper alloys and composites in journal bearings applications. There are several ways to establish a good tribological study through theoretical approaches and computational simulations, but experimental analysis remains decisively essential. There are several tribological experimental setups, including the pin-on-disc test, which is specifically concerned with the study of conformal contacts, and its applicability for the study of journal bearings is not impaired when considering situations of small radial clearances and large contact areas of the geometry of the concave shaft and convex bearing [21–23].

With the gradual technology evolution, commercial tribometers are available on the market, covering a significant range of tests standard to scientific and industrial interests. However, the normal force applied to this equipment does not usually exceed 200 N, mainly due to the mechanical restrictions of inserting suspended masses. Greater capacity equipment, such as the Plint TE67 manufactured by Phoenix Tribology Ltd, Kingsclere, is equipped with a pneumatic system capable of handling loads of up to 1000 N. Still, this feature is not commonly found among other suppliers [24].

Using self-made dedicated tribometers in tribological research is a relatively common activity, and a recent study, based on publications in the leading tribology journals during a period in 2022, reveals that 34% of researchers used some customized tribometers for their experiments, which are relevant numbers [22].

As the demand for innovative copper alloys and composites continues to rise in heavy machinery applications, it becomes crucial to consider the tribological and thermal effects present in high-load and low-speed conditions. Furthermore, broadening the range of alloys compatible with emerging manufacturing processes and technologies is imperative. The present study aims to disseminate the insights gained from developing, constructing, and validating a custom tribometer, specifically emphasizing these fundamental principles and

discussing tribological results obtained from testing high-lead bronze and nickel aluminum bronze alloys.

2. Materials and Methods

This work encompasses all project stages, including the inception of fundamental principles, equipment design, and construction (Section 2.1), results validation (Section 2.2), and an in-depth tribological behavior study of two commercial copper alloys in a wide range of tribological tests, using various PV factors in this developed equipment (Section 2.3).

2.1. Design and Construction

Figure 1 shows an overview of the external design, and Figure 2 details the main tribometer parts. Considering the high specific loads of interest, a design for applying loads using two pneumatic actuators with a combined load capacity of up to 784 N was chosen.

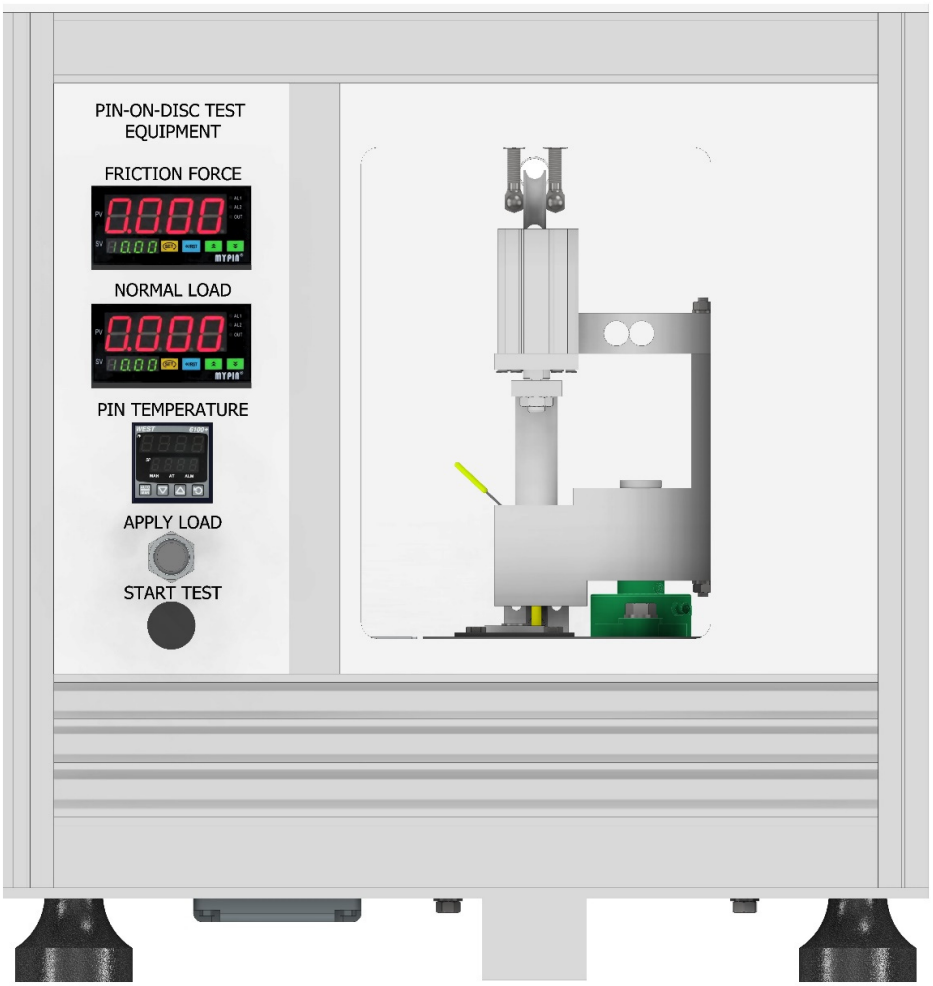

Figure 1. Tribometer overall external design.

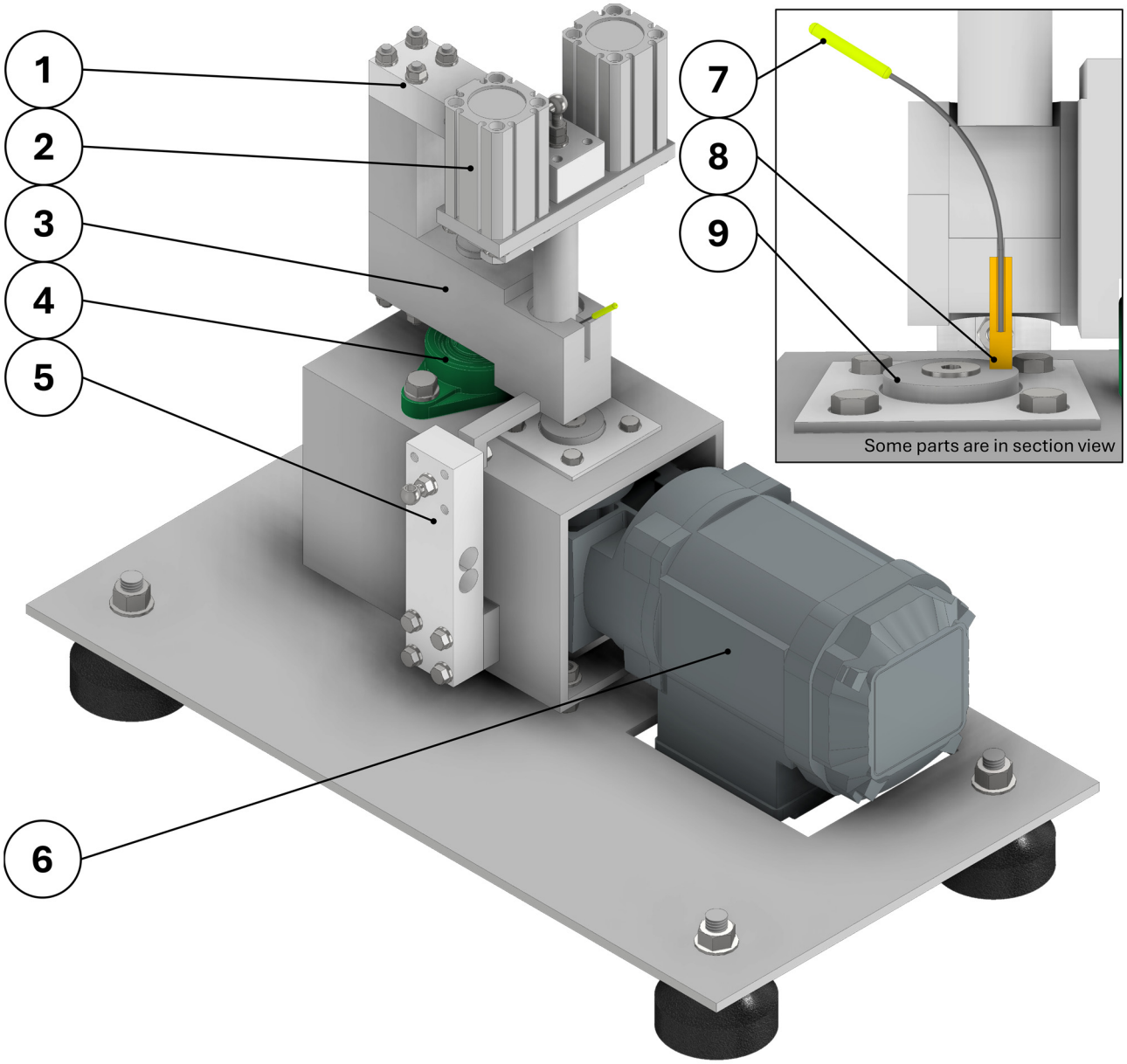

Figure 2. Main tribometer parts: (1) 4-wire load cell for normal load, (2) pneumatic actuator, (3) base, (4) axial ball bearing, (5) 4-wire load cell for friction force, (6) geared motor, (7) type J Ø1.5 mm thermocouple, (8) pin of test material, (9) steel disc.

Support for a Ø6.00 mm pin was developed to receive a Ø1.5 mm Type-J thermocouple. This thermocouple was chosen because its operating range is compatible with the expected temperature ranges for the tribological test and is associated with higher sensitivity and fast response. The support is mounted in a robust base with two axial ball bearings to significantly reduce the existing friction, whose force vector component could impair the friction force results. The concept designed for the support allows for a wide variety of different lengths for the pin, which can vary from 10 to up to 60 mm, and the pin diameter can be changed by replacing the pin holder.

AISI 1045 steel disc with a diameter of 36 mm and a thickness of 5 mm was selected as a counter face. The maximum allowable deviation from parallelism is 0.01 mm. However, any other alloy can be used since it is not restricted. This material is chosen because of its widespread use as heavy equipment shafts. The dimensions of the disc and pin holder

result in a 13 mm radius for the wear track. The disc support shaft is rotated by a geared motor with a maximum output of 207 rpm.

Figure 3 details the communication system, with proper real-time recording of results. The Ø1.5 mm Type-J thermocouple is linked with a digital temperature controller with a 4–20 mA analog output for pin temperature recording. To record real-time measurements of normal and friction force values, two aluminum single-point load cells were used, with dimensions of 149 × 37 × 24.5 mm, maximum capacity of 1982 N, and resolution of 0.0981 N, linked individually to a 4–20 mA analog converter.

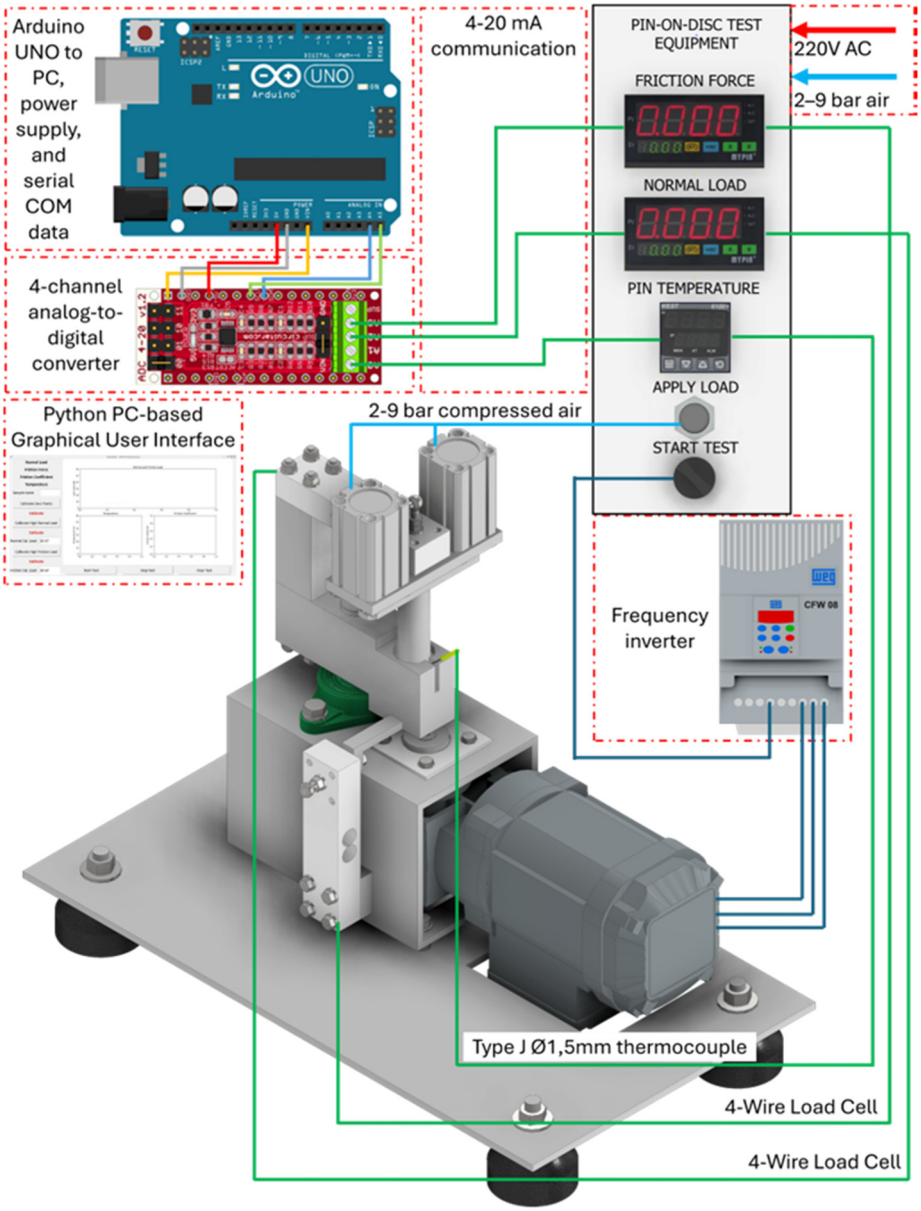

Figure 3. Tribometer communication protocol.

The three 4–20 mA signals are sent to a 4-channel analog–digital converter (ADC) with 16 bits of resolution, allowing a maximum of 860 samples per second. A frequency inverter controls the disc rotation, and the pneumatic actuator pressure is manually adjusted using a pneumatic regulator. The ADC is connected to an Arduino UNO, and programming was done to establish serial communication at an acquisition rate of 10 samples per second.

Arduino UNO is connected to a PC serial port, and a Python-based GUI accesses data via this communication protocol, allowing graphical monitoring of the test outcomes. Additionally, information from the serial port is saved in a .csv file for future analysis.

2.2. Results Validation Approaches

Two approaches were taken to validate the tribometer's developed results: one focusing on estimating the equipment measurement uncertainties (Section 2.2.1) and the other on comparative results with different equipment (Section 2.2.2).

2.2.1. Uncertainty Friction Coefficient Estimation Methodology

The primary sources of uncertainty were studied to evaluate the measurement uncertainty of the tribometer's friction coefficient, categorized into Type A and Type B [25,26].

Type A uncertainties were determined when the measurement was repeated under the same conditions, and the statistical methods were applied to the measured values. Based on this, the defined load cell calibration approach consists of a calibrated mass suspended by steel cables, as shown in Figure 4. To guarantee the system's stiffness, it has been secured to an aluminum structure forming part of the equipment's fairing, thus contributing to a compact design. In addition, the system has been placed on a level base equipped with vibration dampers to safeguard against any potential external effects during testing [25,26].

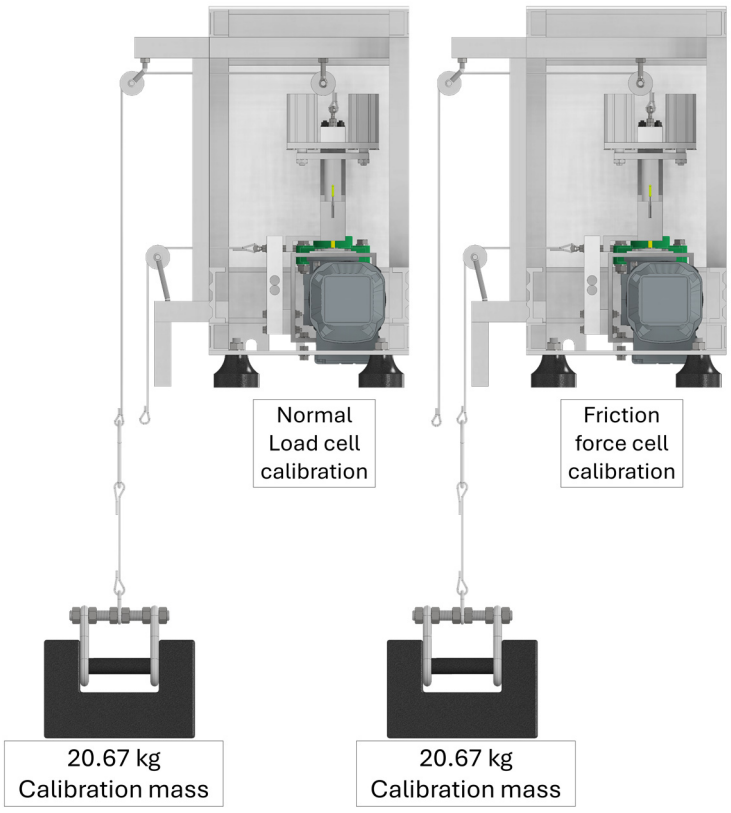

Figure 4. Load cells calibration apparatus.

The evaluation procedure considered 24 measurements of normal and friction forces, each after unloading and load steps, using a 20.67 kg standard mass. Type A uncertainty in these conditions can be associated with standard deviation of the mean and expressed as (3) [26]:

$$u(x_i) = S(\overline{X}_i) = \left(\frac{1}{n(n-1)} \sum_{k=1}^{n} \left(X_{i,k} - \overline{X} \right)^2 \right)^{\frac{1}{2}} \quad (3)$$

The Type B evaluation of standard uncertainty typically depends on scientific expertise. It considers all the relevant information accessible, including manufacturer specifications, data provided in calibration, and other reports. Comprehensive error, output error, nonlinearity error, and instrument resolution were considered from manufacturer data. Due to analog–digital conversion and the complexity of defining how measurement uncertainty is distributed, a reasonable default model for all Type B uncertainty components (a) is a rectangular distribution, and can be estimated by (4) [25,26].

$$u(x_i) = \frac{a}{\sqrt{3}} \tag{4}$$

The combined standard uncertainty of the measurement result, designated by $u_c(y)$, is taken to represent the estimated standard deviation of the result. Given that measurements are evaluated independently, i.e., zero covariance, the second component of the equation is disregarded and takes the form (5) [25,26].

$$u_c{}^2(y) = \sum_{i=1}^{N} \left(\frac{\partial f}{\partial x_i}\right)^2 \cdot u^2(x_i) \tag{5}$$

Considering the friction coefficient equation as $\mu = F/W$, a suitable equation to define uncertainty can be expressed from (5) as (6) [25]:

$$u_\mu{}^2 = \left(\frac{1}{W}\right)^2 \cdot u_F{}^2 + \left(\frac{F}{W^2}\right)^2 \cdot u_W{}^2 \tag{6}$$

2.2.2. Comparative Study of the Results with Reference Equipment

Knowing that tribological tests are destructive, they cannot be repeated under the repeatability conditions stated, the uncertainties Type A cannot be evaluated, and the reproducibility of tribological tests is far from trivial [27].

Aware of this limitation, the results of the pin-on-disc test were compared between two different pieces of equipment. For this purpose, a Plint TE-66 pin-on-disc tribometer was chosen [24].

The tests were carried out in triplicate using two copper alloys: a nickel aluminum bronze (NAB) obtained through the industrial process of continuous casting, hot extruded at 900 °C, light draw and stress relived at 600 °C, and an industrially manufactured continuous cast high-lead bronze (HLB), with respective chemical compositions detailed in Table 1.

Table 1. Chemical composition of evaluated materials (%wt.).

Designation	Al	Ni	Fe	Pb	Zn	Sn	Cu
NAB	11	4	5	-	-	-	Remainder
HLB	-	-	-	15	8	4	Remainder

Both sets of samples were prepared from Ø50 mm bars in EDM to Ø6 × 30 mm pins, and every contact face was carefully surfaced with 200, 400, and 600 grit sandpaper to ensure the best contact condition between the pin and disc.

Ø36 × 5 mm 1045 steel disc, with a hardness of 246.17 ± 7.4 HV, was ground on both sides to obtain a maximum parallelism deviation of 0.01 mm and Ra roughness of 0.624 ± 0.11 µm.

Pins and discs were ultrasonically cleaned in acetone for 20 min and dried for 10 min at 60 °C. Posteriorly, they were measured on a 0.0001 g precision analytical balance. The comparative test, whose parameters are in Table 2, was carried out in both equipment (custom and reference) in dry sliding conditions, with a load of 580.07 N, a rotation of 80 rpm, and a 13 mm track radius.

Table 2. Comparative tribological tests.

Test	W [N]	P [MPa]	V [m/s]	PV [MPa·m·s^{-1}]	Test [s]	Sliding Distance [m]
Comparative	580.07	20.52	0.11	2.2	3600	388.32

After the test, the pins and discs were subjected to the same cleaning and drying procedure and weighed again to evaluate the specific wear rate (k), defined as the worn material volume (Q) per unit of sliding distance (L_s) and per unit of load (W) of normal contact (Equation (7)) [1,5].

$$k = \frac{Q}{L_s \cdot W} \quad (7)$$

2.3. Tribological Performance Study of Two Commercial Copper Alloys Methodology

Before conducting tribological tests, physical, mechanical, and metallographic evaluations were performed on two copper alloys under high loads and low sliding speeds using the developed equipment. The same alloys presented in Table 1 and Ø36 × 5 mm 1045 steel discs described in Section 2.2.2 were used. The samples were first analyzed using the pycnometer density test and HV_{10} hardness test. Optical microscopy observation was performed using $FeCl_3$ etching solution on HLB and as polished on NAB to identify the phases.

The tribological evaluation was divided into three sections. Section 2.3.1 presented details of the tribological tests. Section 2.3.2 evaluated the effect of temperature on tribological performance. Section 2.3.3 studied subsurface strain during dry sliding.

2.3.1. Tribological Tests Definitions

Tribological tests were conducted on all samples for both HLB and NAB. These tests included three normal load levels, named L (Low–289.89 N), M (Medium–580.07 N), and H (High–755.37 N), and five PV factor levels (1.1 to 5.0 in MPa·m·s^{-1}), as detailed in Table 3. The tests were performed in triplicate using developed equipment. During the tests, the friction coefficient values were continuously recorded.

Table 3. Tribological tests.

Test	W [N]	P [MPa]	V [m/s]	PV [MPa·m·s^{-1}]	Test [s]	Sliding Distance [m]
PV-1.1L	289.89	10.25	0.11	1.1	3600	388.32
PV-1.1M	580.07	20.52	0.05	1.1	7200	388.32
PV-1.1H	755.37	26.72	0.04	1.1	9381	388.31
PV-2.2L	289.89	10.25	0.21	2.2	1800	388.32
PV-2.2M	580.07	20.52	0.11	2.2	3600	388.32
PV-2.2H	755.37	26.72	0.08	2.2	4691	388.36
PV-2.9L	289.89	10.25	0.28	2.9	1382	388.52
PV-2.9M	580.07	20.52	0.14	2.9	2764	388.33
PV-2.0H	755.37	26.72	0.11	2.9	3600	388.32
PV-4.0M	580.07	20.52	0.19	4.0	2011	388.29
PV-4.0H	755.37	26.72	0.15	4.0	2618	388.29
PV-5.0M	580.07	20.52	0.24	5.0	1609	388.33
PV-5.0H	755.37	26.72	0.19	5.0	2095	388.40

The specific wear rate was obtained using the same cleaning, preparation, and weighing procedure described in Section 2.2.2. The debris generated during the test was collected and comparatively analyzed by SEM.

2.3.2. Effects of Temperature on Tribological Performance Study

As already mentioned, due to the expected relevance of thermal effects in the tribological conditions involved in dry sliding, using the same materials and the same procedure for preparing the pins described in Section 2.2.2, a Ø1.5 × 20 mm hole was made on the opposite side to receive an embedded Type-J thermocouple starting positioned at 10 mm from the sliding contact region.

A prediction of bulk temperature increase from room temperature ($T_b - T_0$) during dry sliding in a pin-on-disc test is a work that received several contributions [28–41]. During friction tests, the pin remains in constant contact with the disc. The pin temperature fluctuates significantly in the initial stages until it stabilizes and reaches a steady state. From this point, conduction is the primary mode of heat transfer. Based on this assumption and ignoring heat lost by emission, Ashby et al. [31] proposed Equation (8). It considers the total heat per area generation as a sum of the pin and disc heat per area (respectively q_1 and q_2). These calculations involve considering the pin and disc materials' thermal conductivity (k_1 and k_2) and the two equivalent linear heat diffusion lengths (l_{1b} and l_{2b}) for the pin and disc, respectively.

$$q = \mu \cdot P \cdot V = q_1 + q_2 = \frac{k_1}{l_{1b}}(T_b - T_0) + \frac{k_2}{l_{2b}}(T_b - T_0) \quad (8)$$

l_{1b} can be determined by (9), being l_1 the linear distance of sliding contact and pin support, A_n nominal contact area, and A_{c1} the nominal contact area of the clamp contact. L_{2b} is determined by (10), being r_0 the radius of the nominal contact area [31].

$$l_{1b} = l_1 + \frac{A_n \cdot k_1}{A_{c1} \cdot h_{c1}} \quad (9)$$

$$l_{2b} = \frac{\pi^{\frac{1}{2}} \cdot r_0}{2} \quad (10)$$

The heat transfer coefficient, denoted by h_{c1}, is related to the convective heat extraction, and can be approximated using (11). ω represents the angular velocity. [33]

$$h_{c1} = 2.25 \cdot \sqrt{\omega} \quad (11)$$

Bulk temperature increase ($T_b - T_0$) is determined from algebraic manipulation of (8) in form (12): [31]

$$T_b - T_0 = \mu \cdot P \cdot V \cdot \left(\frac{1}{\frac{k_1}{l_{1b}} + \frac{k_2}{l_{2b}}} \right) \quad (12)$$

2.3.3. Subsurface Strain during Dry Sliding Study Methodology

When the normal load is high, and the sliding velocity is low, severe mechanical damage is expected due to higher mechanical stresses, with a predominantly plastic wear mechanism. Therefore, it is crucial to assess the subsurface strain (ε) during dry sliding [5,42].

Frictional forces cause strains beneath the surface of metals that can be analyzed through metallographic examination of longitudinally prepared samples. The examination focuses on the tribologically transformed zone (TTZ), which consists of three distinct regions. The first zone is the unaltered bulk material, the second zone has undergone plastic strain due to shear, and the third zone contains metallic oxides with refined submicrometric grains and additional chemical elements, according to Figure 5a [43–47].

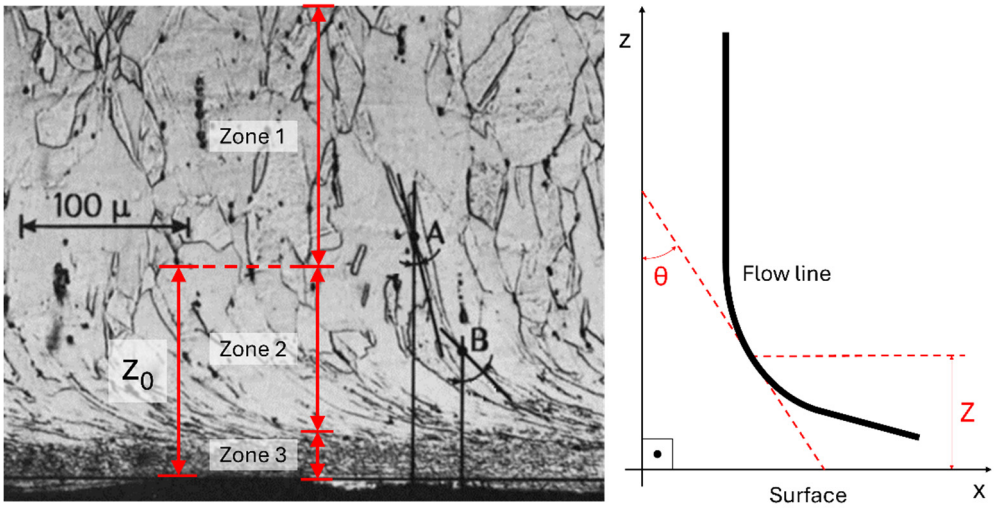

(**a**) (**b**)

Figure 5. (**a**) TTZ zones, (**b**) shear angle (θ) measurement.

To measure subsurface shear strain (ε(Z)) in TTZ, a shear angle (θ) can be measured at different depths (Z) from the worn surface by tracing these lines separately, as explained in Figure 5b [41,44–46].

Equation (13) provides a mathematical interpretation of ε(Z). A geometrical approach determines this value by calculating the average linear intercepts of the deformed and original grain. This assumes a spherical metal grain model deformed due to shear stress. The cross-section that passes through the sphere's center and is perpendicular to the shear stress plane is considered [43,44,46].

$$\varepsilon(Z) = \frac{\sqrt{3}}{3} \cdot \tan[\theta(Z)] \tag{13}$$

3. Results and Discussion

3.1. Design and Construction of the Custom Tribometer

Figure 6a shows the self-made tribometer, and Figure 6b shows equipment used during the calibration step.

(**a**) (**b**)

Figure 6. (**a**) Custom tribometer, (**b**) custom tribometer in the calibration step.

3.2. Validation

3.2.1. Uncertainty Friction Coefficient Estimation

The uncertainty components, their inferred probability distributions, and the coverage actor of the normal force (W) are presented in Table 4, and those of the friction force (F) in Table 5. The combined uncertainty, i.e., the root of the quadratic sum of the uncertainty components of W, resulted in 0.042 kg, and the frictional force was 0.041 kg. Applying these results to Equation (5) and expanding this uncertainty by a factor k = 2, we have an uncertainty estimate value for the friction coefficient of 0.4%. An extensive number of variables can interfere with tribological results; however, it is possible to state that the equipment built within the proposed premises has a negligible effect on the computed μ.

Table 4. Uncertainty components for normal load (W).

Uncertainty Component	a [kg]	Probability Distribution	Coverage Factor	u(xi) [kg]
Type A uncertainty	0.009616	Normal	1	0.009616
Comprehensive error	0.04	Rectangular	$\sqrt{3}$	0.023094011
Output error	0.04	Rectangular	$\sqrt{3}$	0.023094011
Nonlinearity error	0.04	Rectangular	$\sqrt{3}$	0.023094011
Instrument resolution	0.01	Rectangular	$\sqrt{3}$	0.005773503

Table 5. Uncertainty components for friction force (F).

Uncertainty Component	a [kg]	Probability Distribution	Coverage Factor	u(xi) [kg]
Type A uncertainty	0.006295	Normal	1	0.006295
Comprehensive error	0.04	Rectangular	$\sqrt{3}$	0.023094011
Output error	0.04	Rectangular	$\sqrt{3}$	0.023094011
Nonlinearity error	0.04	Rectangular	$\sqrt{3}$	0.023094011
Instrument resolution	0.01	Rectangular	$\sqrt{3}$	0.005773503

3.2.2. Comparative Results with Reference Equipment

Table 6 displays the average and relative standard deviation of the friction coefficient and specific wear rate for the two types of equipment on two different materials. The difference in group average is similar to the relative standard deviation within the group. Figure 7 shows the box plot graphs, which indicate the same. Figure 8 illustrates the progression of the friction coefficient in each group, with expected fluctuations in values. Furthermore, these variations, being of the same order of magnitude in both equipment, lead to the understanding that the source of the variability is in the samples, and the equipment difference is not a probable variation source in this aspect. It is important to note that the tests are destructive, making repeatability more complex. Therefore, at least one triplicate test is necessary, as recommended by Blau [27]. Future interlaboratory proficiency studies in a broader range of tribological conditions are possible.

Table 6. Comparative test results.

Test	μ Mean	μ Relative Standard Deviation	Difference between Group Means	Specific Wear Rate	Difference between Group Means
HLB–Ref.	0.127	7.1%	-	3.9×10^{-7}	-
HLB–T.W.	0.134	4.5%	5.5%	3.5×10^{-7}	11%
NAB–Ref.	0.247	5.7%	-	9.1×10^{-8}	-
NAB–T.W.	0.254	7.9%	2.8%	5.6×10^{-8}	38%

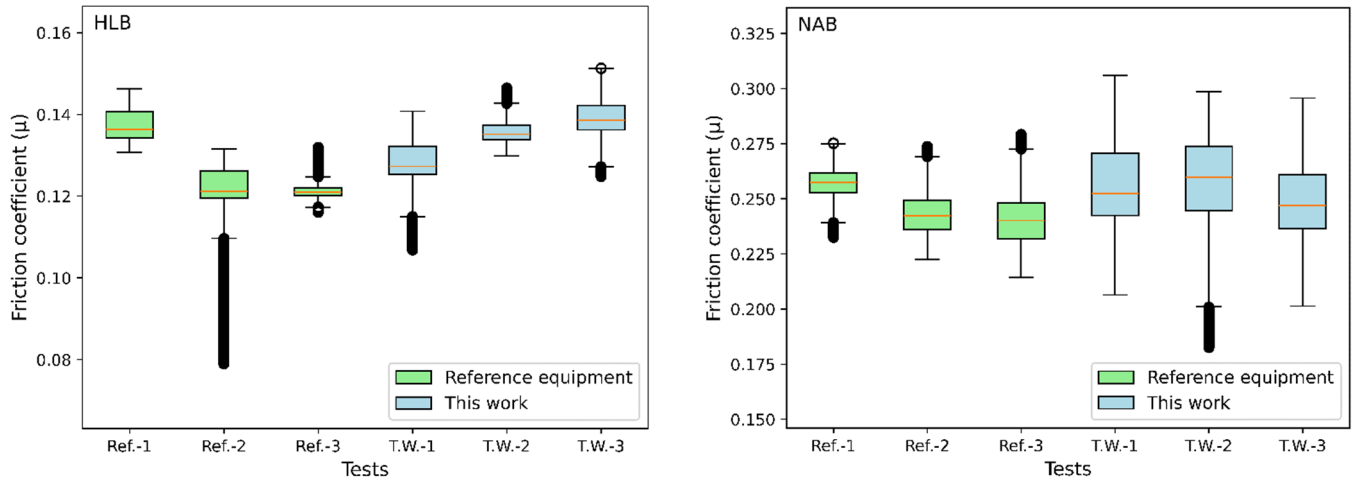

(**a**) (**b**)

Figure 7. Comparative box plot of friction coefficient. (**a**) HLB alloy, (**b**) NAB alloy.

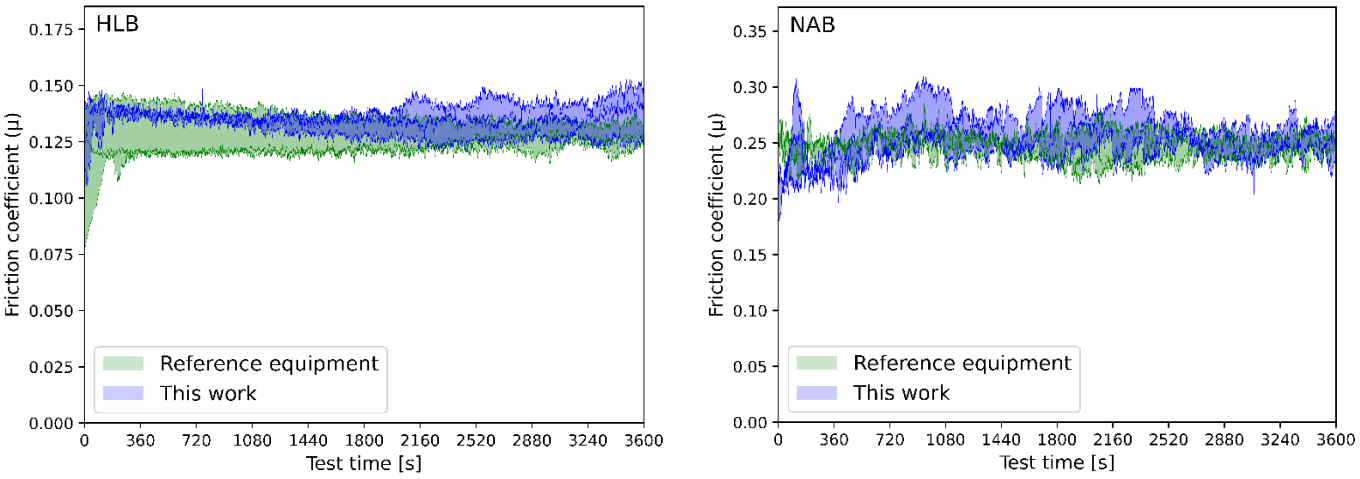

(**a**) (**b**)

Figure 8. Comparative friction coefficient along time. (**a**) HLB alloy, (**b**) NAB alloy.

3.3. Tribological Performance Study of Two Commercial Copper Alloys

Table 7 presents the measured HV_{10} hardness and density values. Thermal conductivity values were taken from refs [14,48]. Regarding the microstructures obtained, the HLB material (Figure 9a) shows a typical microstructure resulting from the continuous casting process it underwent. It consists of an alpha matrix rich in copper with delta phase precipitates rich in tin and lead globules dispersed throughout the dendritic formations. This is similar to what was reported by Glaeser [13] and Prasad [12]. On the other hand, in NAB (Figure 9b), phase formations κ_{II}, κ_{III}, and κ_{IV} can be observed, according to what was published by Hasan [19], Jahanafrooz [16], Wharton et al. [17], and Nascimento et al. [20].

Table 7. Properties of evaluated materials (%wt.).

Material	Hardness [HV_{10}]	Density [kgm^{-3}]	Thermal Conductivity [$W\ m^{-1}\ K^{-1}$]
HLB	65.2	9210	52
NAB	193.8	7510	42

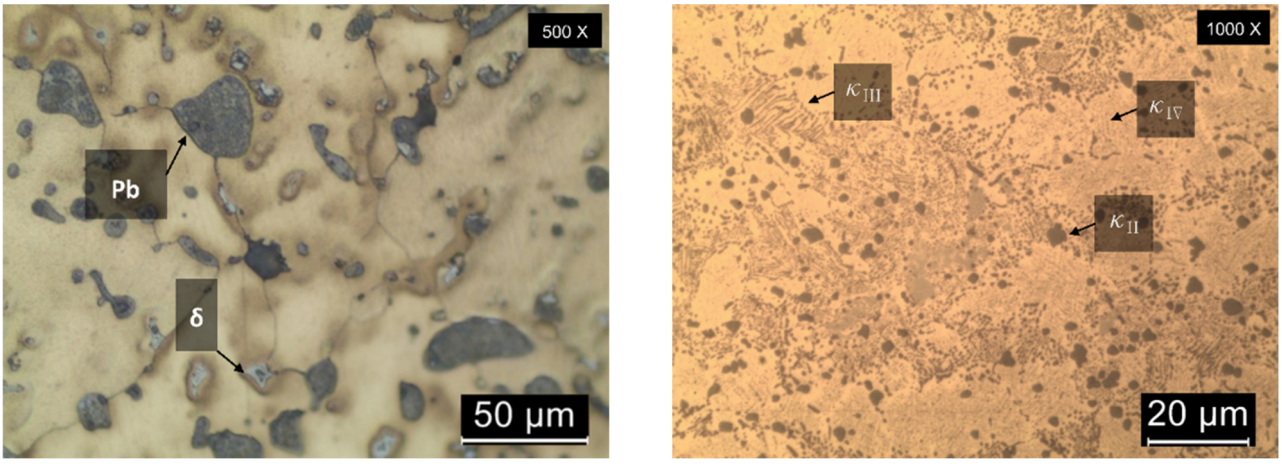

(**a**) (**b**)

Figure 9. HLB microstructure (**a**) and NAB microstructure (**b**). Optical microscopy.

3.3.1. Tribological Tests

The results of the friction coefficient, plotted as a function of pressure and velocity, are presented in Figure 10, with the dashed lines corresponding to the same PV factor and black dots representing each test described in Table 3. The results for the HLB material (Figure 10a) showed a reduction trend with an increase in the PV factor, mainly because of the frictional heating that causes effective smearing of the Pb, which acts as a lubricant phase. The opposite effect is observed in NAB (Figure 10b), with the friction coefficient increasing considerably due to the higher PV factors applied, and a sharp increase in the friction coefficient was observed in the NAB at PV 5.0 tests, which will be further discussed in the results in Section 3.3.2.

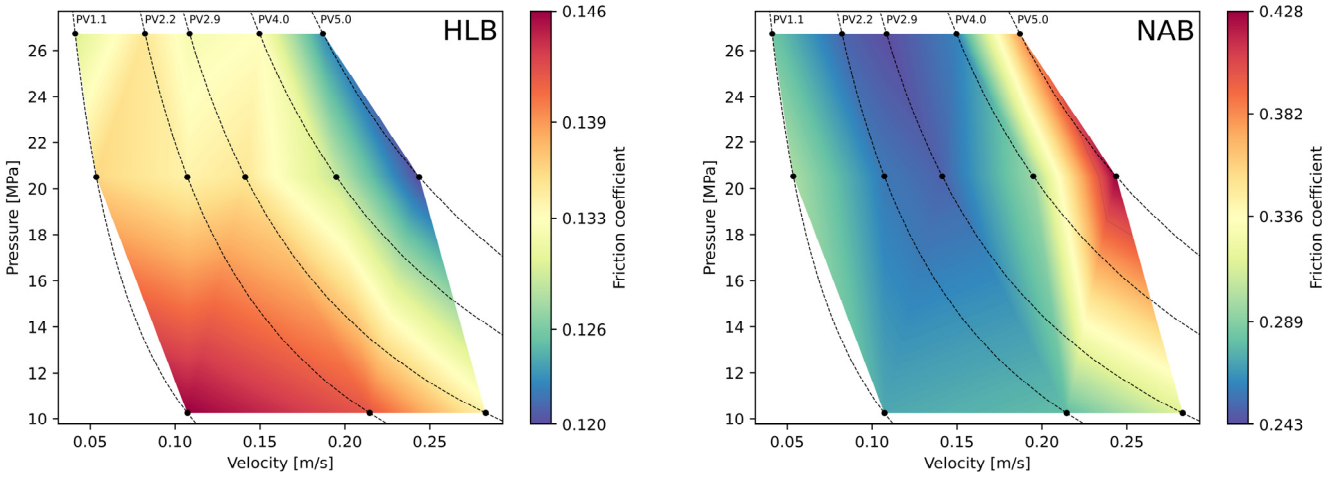

(**a**) (**b**)

Figure 10. Comparative friction coefficient. (**a**) HLB alloy, (**b**) NAB alloy.

The wear rate values (Figure 11) follow a trend where higher PV factors result in higher k values. The HLB results were around 10^{-7}, while NAB showed a significantly lower wear rate of around 10^{-8}. This can be attributed to NAB's higher hardness due to the presence of phases κ_{II}, κ_{III}, and κ_{IV}.

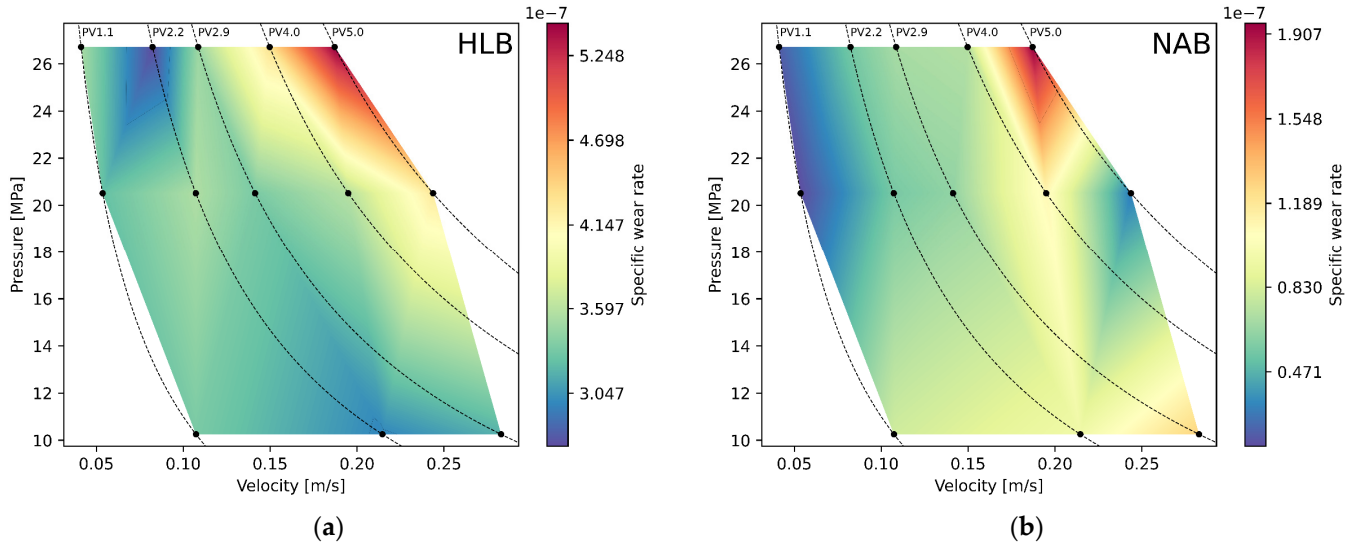

Figure 11. Comparative specific wear rate. (**a**) HLB alloy, (**b**) NAB alloy.

Regarding the debris collected during the test (Figure 12), the debris from the HLB material was generally coarse metal plates with some fine oxide particles, and progressively, the debris and the size of coarse debris increased due to the increase in the PV factor. In the case of NAB, the fraction of oxidized particles is higher, and there is also the presence of coarse debris. These characteristics are directly and consistently related to the delamination wear mechanism, which was expected in the high-load and low-velocity regime. One point identified in some NAB samples was evidence of an additional abrasive wear mechanism, with the formation of ferrous alloy chips. This may be one of the reasons for the sudden increase in the NAB friction coefficient due to the increase in the PV factor. These characteristics lead to a transition from mild to severe wear regime [5,36].

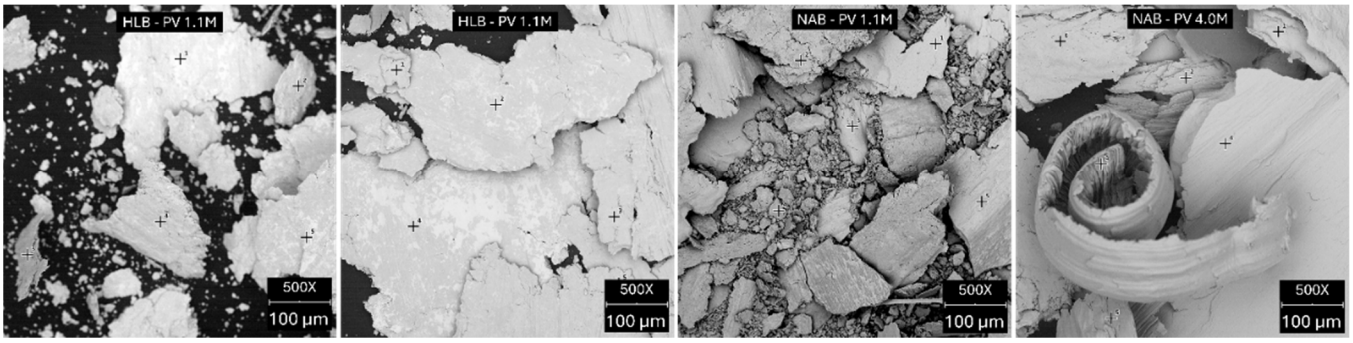

Figure 12. Examples of collected debris after pin-on-disc test. SEM, backscattered electrons.

3.3.2. Effects of Temperature on Tribological Performance

Figure 13 details comparative graphs of the total temperature increase in the pin. Figure 14 shows the temperature variation of one of the replicas of each test as a function of test time. During all the tests, the temperature increased significantly in the first few seconds. This finding is consistent with previous studies [29–41].

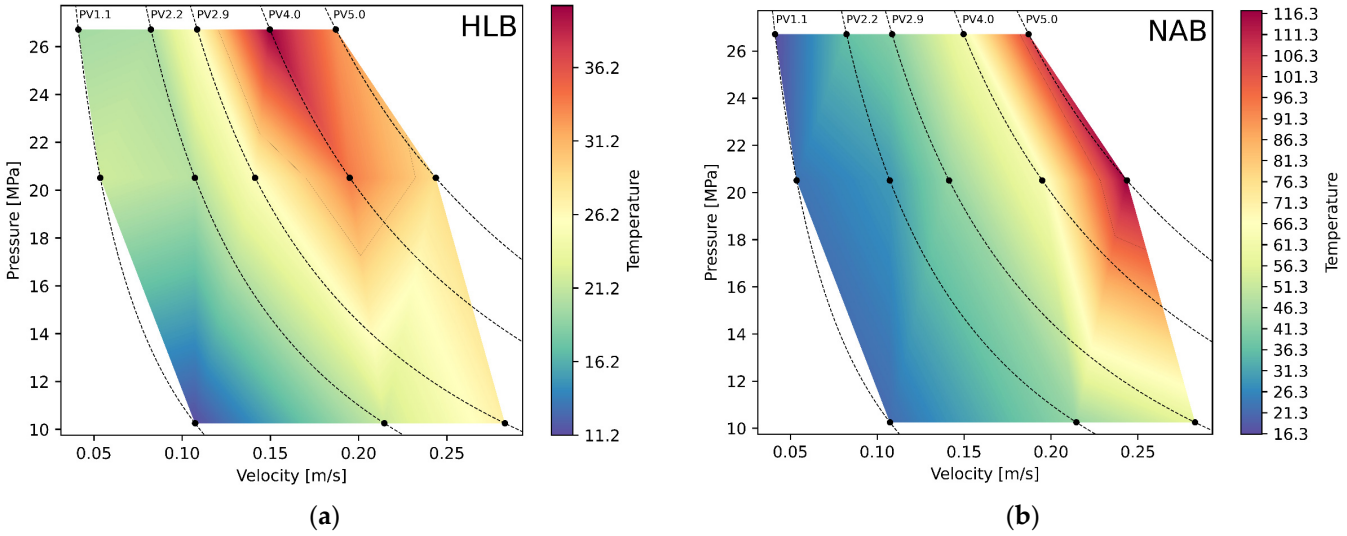

Figure 13. Comparative measured total temperature increase. (**a**) HLB alloy, (**b**) NAB alloy.

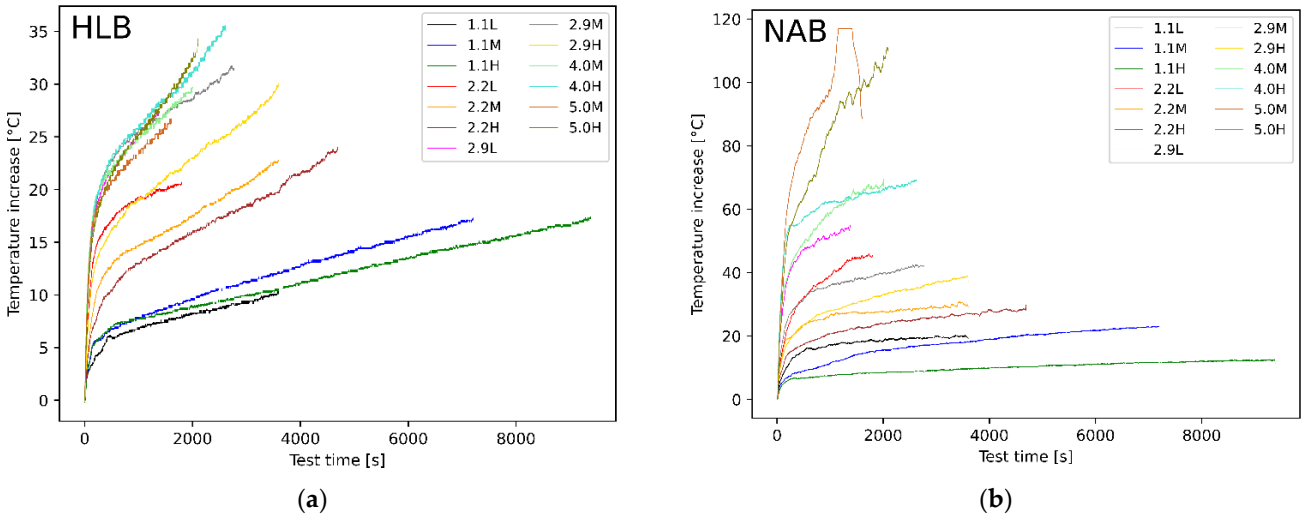

Figure 14. Comparative temperature increases for each test. (**a**) HLB alloy, (**b**) NAB alloy.

Furthermore, the research found that higher PV factors resulted in greater temperature increases. This outcome was expected since higher PV factors generate more energy in the contact area, leading to a rise in temperature. Figure 15 illustrates a significant correlation between the calculated energy values per area entering the test pin (q_1) and the measured temperatures.

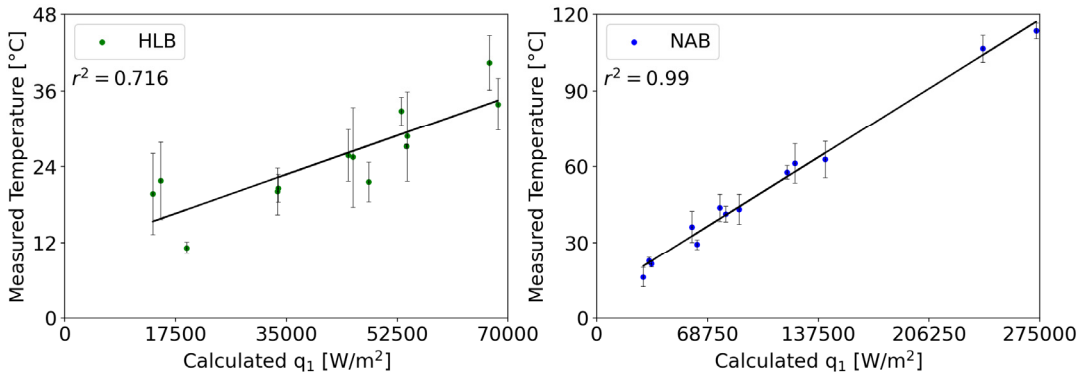

Figure 15. Calculated q_1 versus measured temperature increase.

Figure 16 compares measured and calculated temperatures according to Equation (12). In general, the calculated values are slightly lower, even though the results are within the same order of magnitude. The thermal model adopted is strongly dependent on linear heat diffusion lengths, and according to the author [31], experimental results can be used to fine-tune the results.

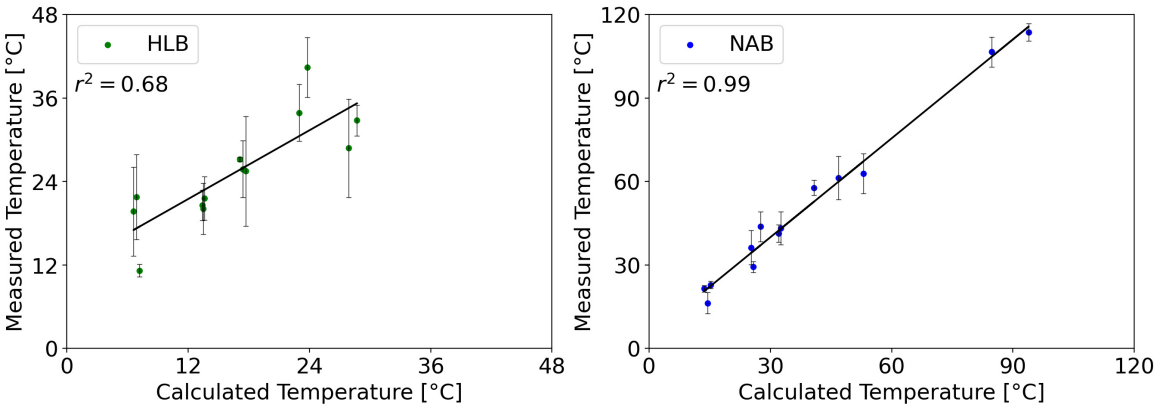

Figure 16. Calculated temperature increase versus measured temperature increase.

A significant correlation coefficient was found between the measured and calculated temperature values, particularly for the NAB alloy. While HLB exhibited a slightly lower correlation coefficient, it followed a similar trend and was consistent with the theoretical model outlined in Equation (12). Temperature measurement in tribological tests is known to be complex, as discussed in another research [47]. However, there are opportunities to improve temperature measurement, and, consequently, the thermal model for the specific conditions addressed in this study, for instance, by employing numerical simulation.

3.3.3. Subsurface Strain during Dry Sliding

Figure 17 presents the plotted values of the subsurface strain calculated according to Equation (13) as a function of the distance from the surface using the micrographs of the subsurface strain in the tested pin samples for the HLB alloy in Figure 18 and for the NAB alloy in Figure 19. In general, the results show that the applied loads induce more significant subsurface strains, and the values for the NAB alloy are considerably greater than those obtained for the HLB alloy. This difference is mainly due to the smearing of the self-lubricating lead particles, and respective low shear strength.

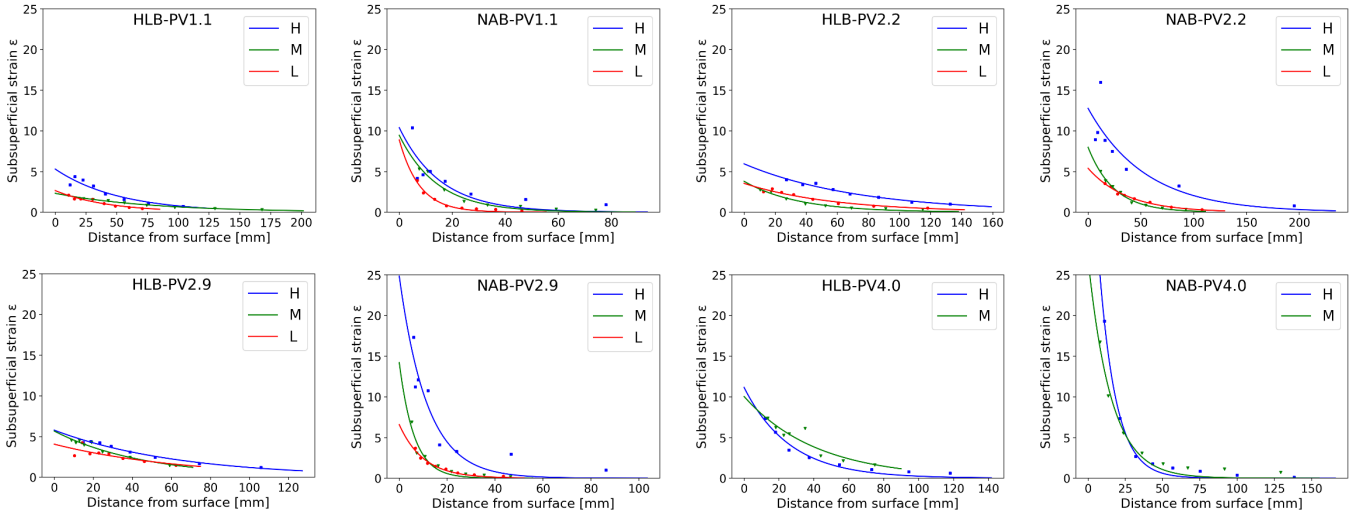

Figure 17. Subsurface strain in different PV regimes.

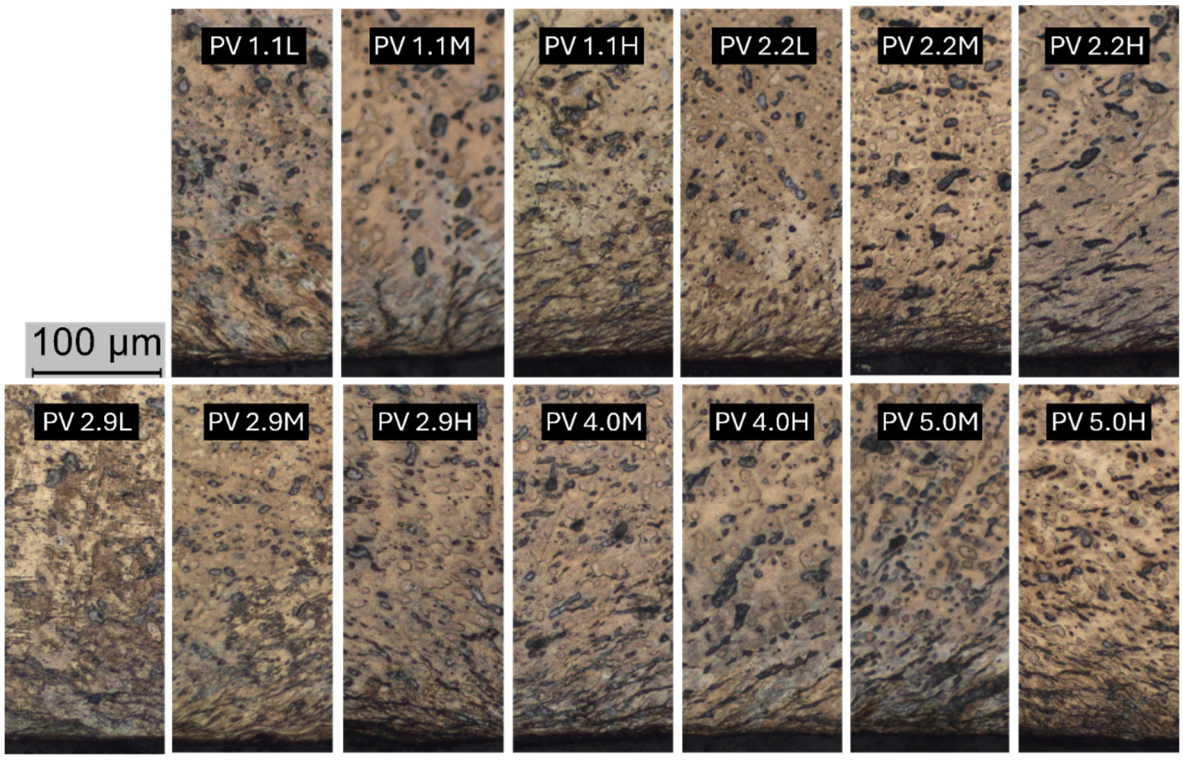

Figure 18. TTZ zone of HLB alloy. Optical microscopy.

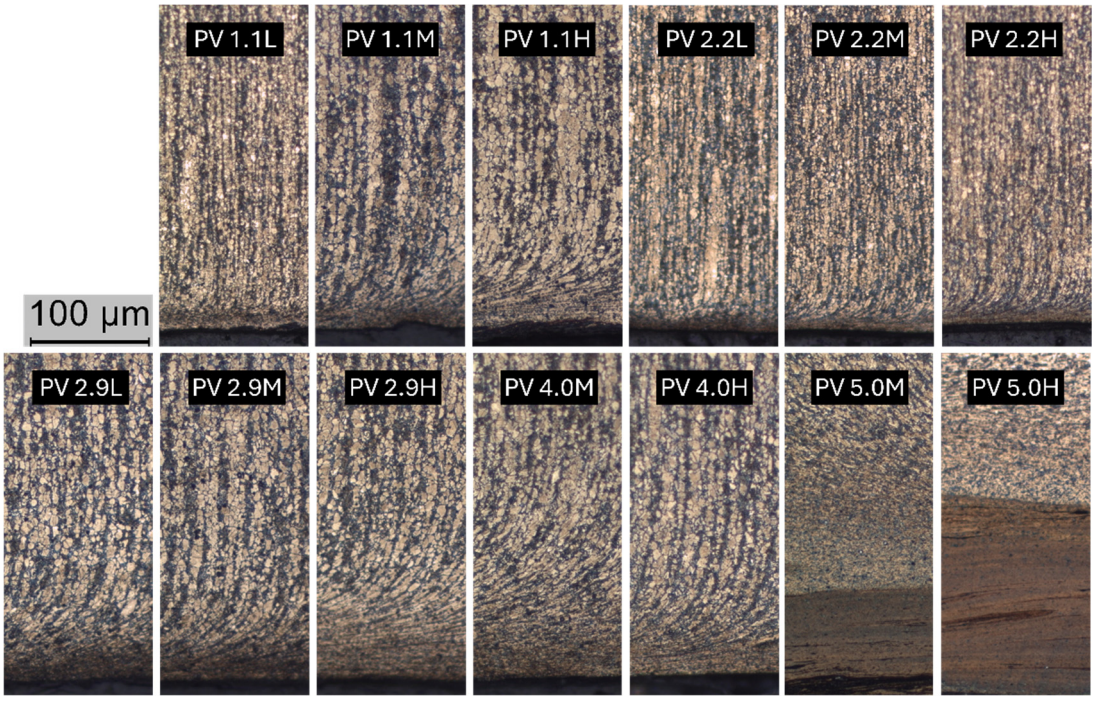

Figure 19. TTZ zone of NAB alloy. Optical microscopy.

The NAB alloy experiences greater energy dissipation due to friction, and this impacts the amount of energy used for plastic strain in the alloy. The evidence of a lower wear rate specific to the NAB alloy shows that debris detachment does not occur as rapidly as observed in the HLB alloy. This leads to a more substantial accumulation of subsurface plastic strain in the NAB alloy. Notably, NAB samples at PV 5.0 factors showed strong

mixed layer formation with high surface oxidation, with evidence of seizure. Due to this, it was not possible to measure the subsurface strain.

4. Conclusions

This work used a custom tribometer to study copper alloys suitable for use in plain bearings, specifically for heavy machines operating at high pressures and low speeds (PV factor). The main concluding remarks are:

The uncertainty estimate value for the friction coefficient of custom equipment is 0.4%, and the equipment built within the proposed premises has a negligible effect on the computed friction coefficient.

The comparison of custom to reference equipment indicates that the variability is attributed to the samples rather than equipment differences. There is the possibility of conducting future proficiency studies under a broader range of tribological conditions.

Significative microstructural differences between NAB and HLB interfere with the observed mechanical and tribological performance, including the lower friction coefficient of HLB due to the insoluble Pb precipitates and the lower specific wear rate of NAB due to the kappa precipitates.

Increasing the PV factor in HLB material reduces the friction coefficient due to frictional heating smearing the Pb, which acts as a lubricant. In contrast, NAB shows a considerable increase in the friction coefficient with higher PV factors, especially at PV 5.0 tests, due to additional abrasive wear.

Measured and calculated temperatures are within the same order of magnitude. NAB measured and calculated temperature values show a strong correlation. Although HLB correlation coefficient is slightly lower, it follows a similar trend and is consistent with the theoretical model. There are opportunities to improve temperature measurement and the thermal model for specific conditions, which could be done through methods like numerical simulation.

The results show that the NAB alloy experiences more significant subsurface strains than the HLB alloy due to the smearing of self-lubricating lead particles with low shear strength. The NAB alloy also dissipates more energy due to friction, causing more significant plastic strain. The lower wear rate in the NAB alloy results in slower debris detachment, leading to a buildup of subsurface plastic strain.

Copper alloys and composites that combine the low friction coefficients of HLB with the high wear resistance of NAB offer an opportunity to develop solid lubricant potential, and an in-depth study of this potential can be carried out.

Author Contributions: M.R.d.S. designed, built, and validated the equipment; M.R.d.S., V.T.d.S., F.G.L. and D.A.S. performed the experiments; M.R.d.S., V.T.d.S., F.G.L., D.A.S. and I.F.M. contributed results analysis; and M.R.d.S. and I.F.M. wrote the paper. All authors have read and agreed to the published version of the manuscript.

Funding: FAPESP, CAPES, and CNPq agencies financially support the Surface Phenomena Laboratory at the University of Sao Paulo.

Data Availability Statement: The raw data supporting the conclusions of this article will be made available by the authors on request.

Acknowledgments: Centro de Pesquisa, Desenvolvimento e Ensaios, da Termomecanica São Paulo S.A. donated materials for analysis and assigned laboratories for analysis.

Conflicts of Interest: The authors declare no conflicts of interest.

Abbreviations

q	Heat per area generation [Wm^{-2}]
μ	Friction coefficient
W	Applied normal load [N]
A	Bearing contact area [m^2]
P	Contact pressure [Pa]
V	Velocity [ms^{-1}]
F	Friction force [N]
k_T	Thermal conductivity of sliding bearing material [$Wm^{-1}K^{-1}$]
s	Thickness of the bearing base material [m]
ΔT	Bearing surface temperature increase [°C]
k	Specific wear rate [$mm^3N^{-1}mm^{-1}$]
L_s	Sliding distance [mm]
Q	Worn material volume [mm^3]
$u(x_i)$	Standard uncertainty
$S(\overline{X}_i)$	Standard deviation of the mean
a	Uncertainty component range value
$u_c(x_i)$	Combined standard uncertainty
u_F	Combined standard uncertainty of friction force
u_W	Combined standard uncertainty of normal load
u_μ	Combined standard uncertainty of friction coefficient
q_1	Pin heat per area generation in pin-on-disc test [Wm^{-2}]
q_2	Disc heat per area generation in pin-on-disc test [Wm^{-2}]
k_1	Pin material thermal conductivity [$Wm^{-1}K^{-1}$]
k_2	Disc material thermal conductivity [$Wm^{-1}K^{-1}$]
l_1	Linear distance of sliding contact and pin support
l_{1b}	Pin heat-diffusion length [m]
l_{2b}	Disc heat-diffusion length [m]
T_b	Surface bulk temperature [°C]
T_0	Room temperature [°C]
A_{c1}	Nominal contact area of the clamp contact [m^2]
A_n	Nominal contact area [m^2]
ω	Angular velocity [s^{-1}]
h_{c1}	Heat transfer coefficient [$Wm^{-2}K^{-1}$]
r_0	Radius of nominal contact area [m]
L	Low load level (289.89N)
M	Medium load level (580.07N)
H	High load level (755.37N)
ε(Z)	Subsurface shear strain in tribologically transformed zone
θ	Shear angle in tribologically transformed zone
Z	Depth from the worn surface

References

1. Kingsbury, G.R. *Friction and Wear of Sliding Bearing Materials*; ASM International: Novelty, OH, USA, 1990.
2. Glaeser, W.A. *Materials for Tribology*; Elsevier Science: Amsterdam, The Netherlands; New York, NY, USA, 1992; 260p.
3. Ruusila, V.; Nyyssönen, T.; Kallio, M.; Vuorinen, P.; Lehtovaara, A.; Valtonen, K.; Kuokkala, V.T. The effect of microstructure and lead content on the tribological properties of bearing alloys. *Proc. Inst. Mech. Eng. Part J J. Eng. Tribol.* **2013**, *227*, 878–887. [CrossRef]
4. Pratt, G.C. Materials for Plain Bearings. *Int. Metall. Rev.* **2013**, *18*, 62–88. [CrossRef]
5. Hutchings, I.M. *Tribology: Friction and Wear of Engineering Materials*; CRC Press: Boca Raton, FL, USA, 1992; 273p.
6. CDA. *Selection Guide with Bound and Hydro Computer-Assisted Sleeve Bearing Design*; Copper Development Association: New York, NY, USA, 1997.
7. CDA. *Cost-Effective Manufacturing: Copper Alloy Bearings (CDA Publication TN45, 1971)*; Copper Development Association: Hempstead, NY, USA, 1992.
8. Prasad, B.K. Sliding wear behaviour of bronzes under varying material composition, microstructure and test conditions. *Wear* **2004**, *257*, 110–123. [CrossRef]

9. Schmidt, R.F.; Schmidt, D.G. Selection and Application of Copper Alloy Castings. In *Properties and Selection: Nonferrous Alloys and Special-Purpose Materials*; ASM International: Novelty, OH, USA, 1990; pp. 346–355.
10. Equey, S.; Houriet, A.; Mischler, S. Wear and frictional mechanisms of copper-based bearing alloys. *Wear* **2011**, *273*, 9–16. [CrossRef]
11. de Gee, A.W.J.; Vaessen, G.H.G.; Begelinger, A. The Influence of Composition and Structure on the Sliding Wear of Copper-Tin-Lead Alloys. *ASLE Trans.* **1969**, *12*, 44–54. [CrossRef]
12. Prasad, B.K.; Patwardhan, A.K.; Yegneswaran, A.H. Factors controlling dry sliding wear behaviour of a leaded tin bronze. *Mater. Sci. Tech. Ser.* **1996**, *12*, 427–435. [CrossRef]
13. Glaeser, W.A. Wear Properties of Heavy Loaded Copper-Base Bearing Alloys. *JOM J. Miner. Met. Mater. Soc.* **1983**, *35*, 50–55. [CrossRef]
14. Richardson, I. *Guide to Nickel Aluminum Bronze for Engineers*; Copper Development Association: Hempstead, NY, USA, 2016.
15. Meigh, H. *Cast and Wrought Aluminium Bronzes: Properties, Processes and Structure*; CRC Press: Boca Raton, FL, USA, 2018.
16. Jahanafrooz, A.; Hasan, F.; Lorimer, G.W.; Ridley, N. Microstructural Development in Complex Nickel-Aluminum Bronzes. *Metall. Trans. A* **1983**, *14*, 1951–1956. [CrossRef]
17. Wharton, J.A.; Barik, R.C.; Kear, G.; Wood, R.J.K.; Stokes, K.R.; Walsh, F.C. The corrosion of nickel–aluminium bronze in seawater. *Corros. Sci.* **2005**, *47*, 3336–3367. [CrossRef]
18. Shi, Z.; Sun, Y.; Bloyce, A.; Bell, T. Unlubricated rolling-sliding wear mechanisms of complex aluminium bronze against steel. *Wear* **1996**, *193*, 235–241. [CrossRef]
19. Hasan, F.; Jahanafrooz, A.; Lorimer, G.W.; Ridley, N. The Morphology, Crystallography, and Chemistry of Phases in as-Cast Nickel-Aluminum Bronze. *Metall. Trans. A* **1982**, *13*, 1337–1345. [CrossRef]
20. Nascimento, M.S.; Santos, G.A.D.; Teram, R.; Santos, V.T.D.; Silva, M.R.D.; Couto, A.A. Effects of Thermal Variables of Solidification on the Microstructure, Hardness, and Microhardness of Cu-Al-Ni-Fe Alloys. *Materials* **2019**, *12*, 1267. [CrossRef]
21. Wang, Q.; Chung, Y.-w. *Encyclopedia of Tribology*; Springer: New York, NY, USA, 2013.
22. Zhou, Y.F.; Tian, Y.; Meng, S.; Zhang, S.L.; Xing, X.L.; Li, D.Y. Open-source tribometer with high repeatability: Development and performance assessment. *Tribol. Int.* **2023**, *184*, 108421. [CrossRef]
23. Lancaster, J.K. Dry bearings: A survey of materials and factors affecting their performance. *Tribology* **1973**, *6*, 219–251. [CrossRef]
24. Phoenix, T. TE67 Pin on Disc Machine. Available online: http://www.phoenix-tribology.com/at2/leaflet/te67 (accessed on 14 May 2024).
25. Novak, R.; Polcar, T. Tribological analysis of thin films by pin-on-disc: Evaluation of friction and wear measurement uncertainty. *Tribol. Int.* **2014**, *74*, 154–163. [CrossRef]
26. Taylor, B.N.; Kuyatt, C.E. *Guidelines for Evaluating and Expressing the Uncertainty of NIST Measurement Results*, 1994 ed.; U.S. Department of Commerce, Technology Administration, National Institute of Standards and Technology: Gaithersburg, MD, USA, 1994; p. 20.
27. Blau, P.J. Lessons learned from the test-to-test variability of different types of wear data. *Wear* **2017**, *376*, 1830–1840. [CrossRef]
28. Bowden, F.P.; Ridler, K.E.W. Physical properties of surfaces-III—The surface temperature of sliding metals—The temperature of lubricated surfaces. *Proc. R. Soc. Lond. Ser. A Math. Phys. Sci.* **1997**, *154*, 640–656. [CrossRef]
29. Kagnaya, T.; Boher, C.; Lambert, L.; Lazard, M.; Cutard, T. Friction at high sliding speed of WC-6Co pin versus steel disc AISI 1045: Estimation of the contact temperature. *Int. J. Multiphysics* **2009**, *3*, 141–153. [CrossRef]
30. Alilat, N.; Baïri, A.; Laraqi, N. Three-dimensional calculation of temperature in a rotating disk subjected to an eccentric circular heat source and surface cooling. *Numer. Heat Transf. Part A* **2004**, *46*, 167–180. [CrossRef]
31. Ashby, M.F.; Abulawi, J.; Kong, H.S. Temperature Maps for Frictional Heating in Dry Sliding. *Tribol. Trans.* **1991**, *34*, 577–587. [CrossRef]
32. Federici, M.; Straffelini, G.; Gialanella, S. Pin-on-Disc Testing of Low-Metallic Friction Material Sliding Against HVOF Coated Cast Iron: Modelling of the Contact Temperature Evolution. *Tribol. Lett.* **2017**, *65*, 121. [CrossRef]
33. Kennedy, F.E.; Lu, Y.; Baker, I. Contact temperatures and their influence on wear during pin-on-disk tribotesting. *Tribol. Int.* **2015**, *82*, 534–542. [CrossRef]
34. Kuhlmannwilsdorf, D. Temperatures at Interfacial Contact Spots—Dependence on Velocity and on Role Reversal of 2 Materials in Sliding Contact. *J. Tribol.* **1987**, *109*, 321–329. [CrossRef]
35. Laraqi, N.; Alilat, N.; de Maria, J.M.G.; Baïri, A. Temperature and division of heat in a pin-on-disc frictional device-Exact analytical solution. *Wear* **2009**, *266*, 765–770. [CrossRef]
36. Lim, S.C.; Ashby, M.F. Overview no.55 Wear-Mechanism Maps. *Acta Metall. Mater.* **1987**, *35*, 1–24. [CrossRef]
37. Straffelini, G.; Verlinski, S.; Verma, P.C.; Valota, G.; Gialanella, S. Wear and Contact Temperature Evolution in Pin-on-Disc Tribotesting of Low-Metallic Friction Material Sliding Against Pearlitic Cast Iron. *Tribol. Lett.* **2016**, *62*, 36. [CrossRef]
38. Tian, X.F.; Kennedy, F.E. Contact Surface-Temperature Models for Finite Bodies in Dry and Boundary Lubricated Sliding. *J. Tribol.* **1993**, *115*, 411–418. [CrossRef]
39. Wang, Y.; Rodkiewicz, C.M. Temperature Maps for Pin-on-Disk Configuration in Dry Sliding. *Tribol. Int.* **1994**, *27*, 259–266. [CrossRef]
40. Yevtushenko, A.; Ukhanska, O.; Chapovska, R. Friction heat distribution between a stationary pin and a rotating disc. *Wear* **1996**, *196*, 219–225. [CrossRef]

41. Kennedy, F.E. Thermal and thermomechanical effects in dry sliding. *Wear* **1984**, *100*, 453–476. [CrossRef]
42. Singh, J.; Alpas, A.T. High-temperature wear and deformation processes in metal matrix composites. *Metall. Mater. Trans. A* **1996**, *27*, 3135–3148. [CrossRef]
43. Alpas, A.T.; Hu, H.; Zhang, J. Plastic-Deformation and Damage Accumulation Below the Worn Surfaces. *Wear* **1993**, *162*, 188–195. [CrossRef]
44. Dautzenberg, J.H.; Zaat, J.H. Quantitative-Determination of Deformation by Sliding Wear. *Wear* **1973**, *23*, 9–19. [CrossRef]
45. Hughes, D.A.; Korellis, J.S. High load sliding, deformation microstructures, strength, and hardening for cutting and metal forming. *Int. J. Mach. Tools Manuf.* **2021**, *168*, 103766. [CrossRef]
46. Menezes, P.L.; Kishore; Kailas, S.V. Subsurface deformation and the role of surface texture—A study with Cu pins and steel plates. *Sadhana* **2008**, *33*, 191–201. [CrossRef]
47. Rice, S.L.; Nowotny, H.; Wayne, S.F. A Survey of the Development of Subsurface Zones in the Wear of Materials. *Key Eng. Mater.* **1991**, *33*, 77–100. [CrossRef]
48. ASM. *Properties and Selection: Nonferrous Alloys and Special-Purpose Materials*; ASM International: Novelty, OH, USA, 1990.